

Towards Photographic Image Manipulation with Balanced Growing of Generative Autoencoders

Ari Heljakka^{1,2} Arno Solin¹ Juho Kannala¹

¹Department of Computer Science, Aalto University, Espoo, Finland

²GenMind Ltd., Espoo, Finland

firstname.lastname@aalto.fi

Abstract

We build on recent advances in progressively growing generative autoencoder models. These models can encode and reconstruct existing images, and generate novel ones, at resolutions comparable to Generative Adversarial Networks (GANs), while consisting only of a single encoder and decoder network. The ability to reconstruct and arbitrarily modify existing samples such as images separates autoencoder models from GANs, but the output quality of image autoencoders has remained inferior. The recently proposed PIONEER autoencoder can reconstruct faces in the 256×256 CELEBA-HQ dataset, but like IntroVAE, another recent method, it often loses the identity of the person in the process. We propose an improved and simplified version of PIONEER and show significantly improved quality and preservation of the face identity in CELEBA-HQ, both visually and quantitatively. We also show evidence of state-of-the-art disentanglement of the latent space of the model, both quantitatively and via realistic image feature manipulations. On the LSUN Bedrooms dataset, our model also improves the results of the original PIONEER. Overall, our results indicate that the PIONEER networks provide a way to photorealistic face manipulation.

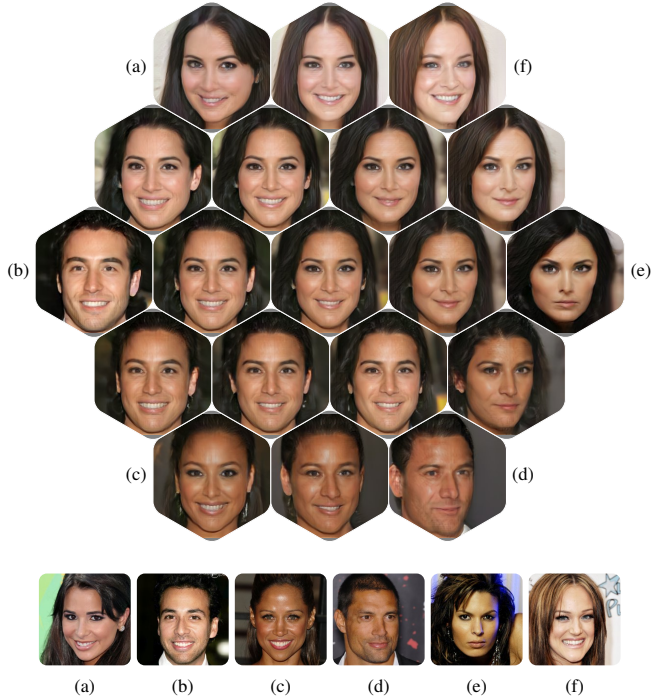


Figure 1. Six-way example interpolations in the latent space between reconstructions of previously unseen input images (bottom) at 256×256 resolution. Best viewed zoomed in.

1. Introduction

Advances in generative image modelling with deep neural networks have raised expectations for delivering new tools for photographic image manipulation and exploration. Generative image modelling involves training the model by a wide variety of data, such as pictures of faces or bedrooms, and allowing it to learn features and structure present in the data. Recent works (e.g. [17, 18, 3]) on using Generative Adversarial Networks (GANs) [9] for images of high quality and resolution have showed that *generating* random beautiful and sharp high-resolution images is achievable by current tools—given a fair deal of engineering and compute.

However, to manipulate existing images and other content, we also need inference, not only the capability to generate random samples. A model that can encode the sample of interest into a well-structured latent space allows us to manipulate the sample via that latent representation (comprising the learned features). In absence of extensions, a GAN has no inference component. In contrast, generative autoencoder models allow both generation and reconstruction, with a bi-directional mapping between the latent feature space and image space. The latent space can be exploited e.g. by interpolating between two or more points that represent images (see Fig. 1), by finding directions that encode an individual

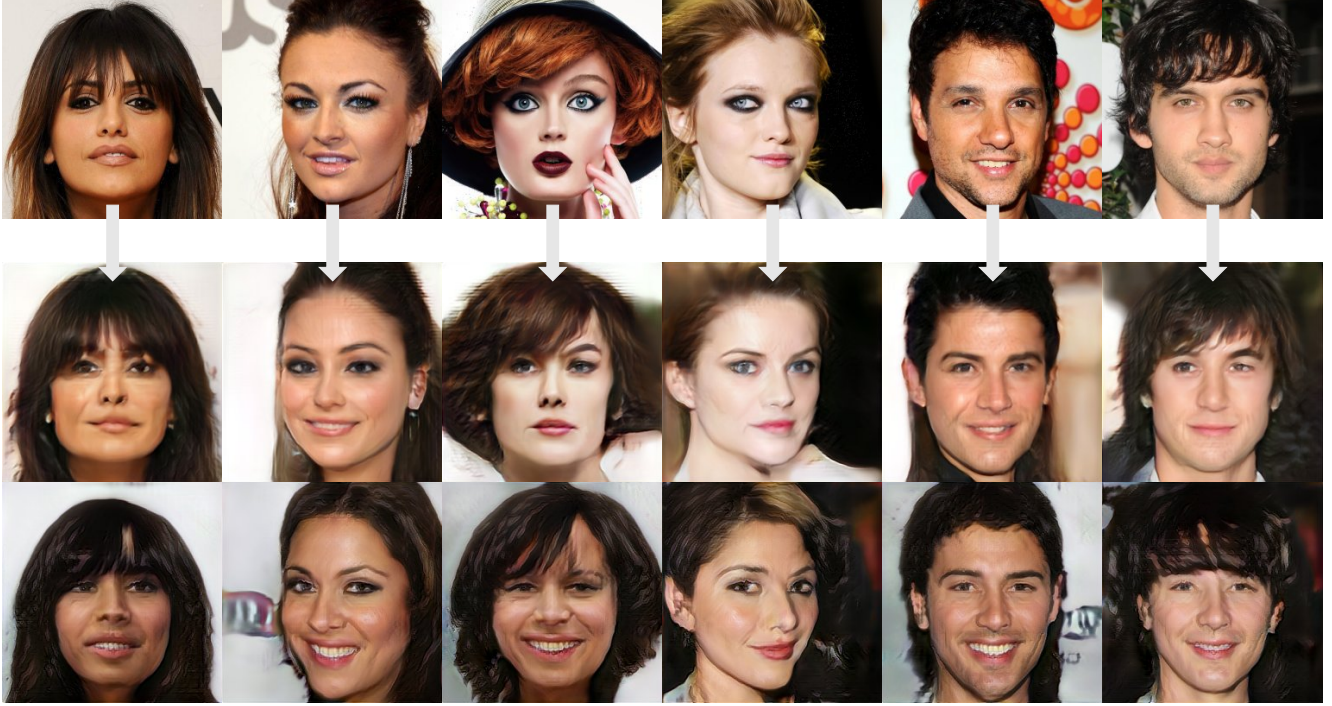


Figure 2. Example of reconstruction quality in 256×256 resolution with typical images from the CELEBA-HQ test set (top row), by our balanced PIONEER (middle) and baseline PIONEER (bottom). Here, the input images are encoded into 512-dimensional latent feature vector and decoded back to the original dimensionality (middle and bottom rows). The encoding–decoding of balanced PIONEER tends to preserve facial features, orientation, expressions, and hair style. Small mistakes can still be observed, especially in male subjects. (Features highly underrepresented in the limited CELEBA-HQ training set, such as a dark-skinned face with atypical orientation, will result in more pronounced failures.)

feature of interest (see Fig. 6) to modify new images, and for other downstream tasks.

The state-of-the-art in this direction was set by three papers simultaneously published in late 2018: the flow-based GLOW method [22], the introspective variational autoencoder (IntroVAE, [14]), and the progressively growing generative autoencoder (PIONEER, [11]) based on the Adversarial Generator–Encoder (AGE, [36]).

In this paper, we build on the progressively growing generative autoencoder concept, primarily the PIONEER network architecture. We seek to balance the training as the model grows progressively towards higher and higher resolutions—a common challenge for generative models (see *e.g.* discussion in [14]). PIONEER was previously shown to reconstruct images only up to 128×128 . With balanced training, our model can generate realistic high resolution images, preserve sample diversity, provide semantically correct reconstructions (Fig. 2), and learn disentangled latent representations of features (Fig. 6).

The contributions and results of this paper are as follows. (i) We first establish a new baseline for PIONEER, with quality and diversity of generated 256×256 samples now close to the state-of-the-art encoder–decoder models and GANs, much improved from the previously published results for the

original version of the method in [11].

(ii) We propose a modified PIONEER model that learns a more accurate representation of the dataset. When reconstructing face images of CELEBA-HQ, the baseline PIONEER often loses the identity. The cause is related to a large dynamic range and occasional collapse of the encoder–decoder minimax game, complicated by three different weight normalization schemes. We are able to drop two out of three, and solve the stability problem by changing the loss function.

(iii) With these improvements, our model can reconstruct 256×256 CELEBA-HQ images with substantially better conservation of identity and significantly improved LPIPS [40] and FID [13] scores. Hence, we show that AGE-based generative models can indeed handle the 256×256 resolution, with performance comparable to the IntroVAE (contrary to what is implied in [14]).

(iv) We show that the latent space of the model allows for realistic face image manipulation, and evaluate it quantitatively with Perceptual Path Length ([18]) metric. We show that even the regular PIONEER is superior to the other baselines, and that our improvements further amplify the difference.

2. Related work

Our work builds upon the previous research in generative image models, such as variational autoencoders (VAEs, [20, 16]), autoregressive models, flow models, and GAN variants. Our approach borrows ideas from both autoencoders and GANs. In this section, we give a brief overview of the background literature and conclude with discussion about the closest related works.

The basic idea of a GAN is to train two networks, generator and discriminator, in a competitive manner so that (a) the generator learns to produce images from the same distribution as the training data and (b) the discriminator learns to distinguish the synthetic images produced by the generator from the real training samples as well as possible. If successful, the generator has become good enough so that the discriminator can no longer make the distinction. The generator starts from a compact random latent code.

During the recent years there has been rapid progress related to GAN-based models and applications. Many recent improvements improve the stability and robustness of the training process by suggesting new loss functions [1], regularization methods [29, 31, 28], multi-resolution training [17, 39], architectures [18], or combinations of these.

However, despite the notable progress in image generation, it is widely accepted that the capability for realistic image synthesis alone is not sufficient for most applications, such as image manipulation, where we start from an existing image. This calls for a model with an encoder, such as a VAE. On the other hand, autoencoders tend to suffer from blurry outputs, and are often used for only low resolution images (even in recent works such as *e.g.* [33, 34, 5], see also comparison in [11]).

Thus, there have been many efforts to combine GANs with autoencoder models, (*e.g.* [4, 30, 7, 8]). For instance, [7] and [8] proposed utilizing three deep networks in order to learn functions that enable mappings between the data space and the latent space in both directions. That is, besides the typical autoencoder architecture, consisting of a decoder (i.e. generator) and encoder networks, their approach uses an additional discriminator network, which is trained to classify tuples of image samples with their latent codes. Other authors introduce additional discriminator networks besides the generator and encoder. For example, [25, 4] use a GAN-like discriminator in sample space and [26, 27] in latent space. Nevertheless, the image synthesis performance of these hybrid models has not yet been shown to match state-of-the-art of purely generative models [17, 18].

In this paper, we build upon PIONEER [11], based on the adversarial generator–encoder (AGE) [36]. In contrast to many other previous works, these two models consist of only two deep networks, a generator and an encoder, which represent the mappings between the image space and latent space. In addition, the method of progressive network

growing, adapted from [17], is utilized in [11].

The results of [11] are promising, and both synthesis and reconstruction have good quality in relatively high image resolutions. However, in this paper, we show that [11] suffers from large fluctuations of the competing divergence terms of the adversarial loss, and this seems to hamper optimization and convergence thereby limiting performance.

Besides [11], other recent and related works are IntroVAE [14] and GLOW [22]. Based on VAE, IntroVAE is fundamentally different from PIONEER that is based on AGE. Based on the contributions of our paper, we are able to show that AGE-based generative models are capable of producing competitive results at 256×256 resolution and with performance comparable to IntroVAE. This is in contrast to the observations in [14], where the authors were not able to make AGE training converge with large image resolutions. This finding is particularly promising since the PIONEER model has a simpler yet more powerful architecture than the corresponding purely generative model PGGAN [17]. It shows that the conventional GAN paradigm of a separate discriminator network is not necessary for learning to infer and generate image data sets.

In terms of image manipulation, we point out that our model learns to manipulate image attributes in a fully unsupervised manner, in contrast to supervised approaches where the class information is provided during training (*e.g.* [24, 12]), and to models only capable of specific discrete domain transformations [42, 19, 37, 6, 15]. In the unsupervised line of work, *e.g.* [5] uses only low resolution, whereas the GAN of [18] shows high resolution, but has no encoder.

3. Methods

In this section, we start from the basics of PIONEER [11] which in turn builds on [36] and [17] (Sec. 3.1). From the perspective of image manipulation in 256×256 resolution (and above), the regular PIONEER reaches reasonable sample quality and diversity, but the reconstructions are often not faithful to the originals (unlike in 128×128 CELEBA).

Therefore, our main task in this paper is to substantially improve the reconstructions without sacrificing other performance aspects. For this, we must address two issues: (i) On the training behavior level, the PIONEER training dynamics are difficult to optimize, due to wildly oscillating Kullback–Leibler divergence (KL) terms during training. Further, occasionally the encoder and decoder completely diverge and the training performance collapses (Fig. 3(a)). (ii) On the algorithmic level, the three different normalization schemes used in baseline PIONEER compound the difficulty of understanding the behavior of the model, and together appear to contribute to the issue (1) in complicated ways. Instead of proposing yet another network architecture, we seek to find the minimum sufficient changes to simplify and stabilise the training workflow.

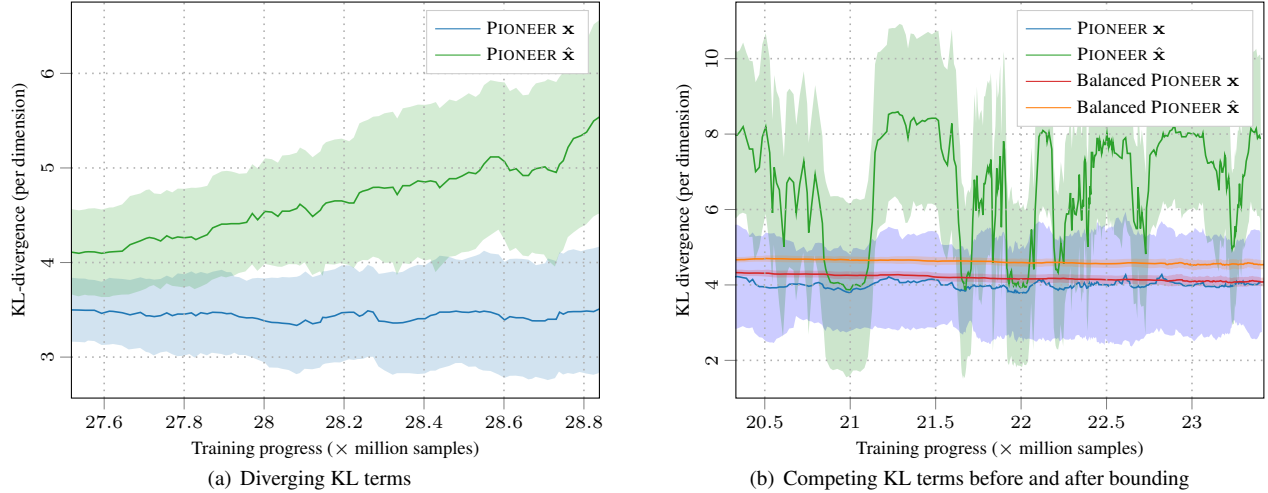


Figure 3. The competing KL divergence terms that the encoder assigns for \mathbf{x} (training samples) and $\hat{\mathbf{x}}$ (generated samples) in PIONEER show two pathological properties. At times, the encoder overpowers the decoder, and the terms begin to diverge (left). Furthermore, after pre-training stages, the dynamic range of the terms is large and ultimately creates an upper bound to the learning capacity, unless we modify the loss function as in Eq. (5) (right). This also results in steadily decreasing magnitude of both terms.

In order to succeed in the main task, we benefit from first simplifying the algorithm, and reduce the three normalization schemes to only one (Sec. 3.2). This simplification comes at the cost of even less stable training dynamics. However, we have now made the behavior more straightforward, and are able to stabilize the training by simply bounding the difference between the competing KL terms, preventing them from diverging (Sec. 3.3).

Finally, in order to confirm our success on the main task, we analyze the representational power of our improved model by measuring the degree of disentanglement in the model’s latent space and demonstrate realistic image feature manipulations (Sec. 3.4).

3.1. Model training dynamics

In PIONEER, the encoder ϕ and decoder θ are trained separately during each training step, with separate loss functions. Because of this separation and the presence of loss terms that are the exact opposites of each other, the training can be called adversarial. With $\mathbf{x} \sim X$ as the training samples and $\hat{\mathbf{x}} = \theta(\hat{\mathbf{z}})$ where $\hat{\mathbf{z}} \sim N(\mathbf{0}, \mathbf{I})$, the encoder loss consists of the encoder trying to push the distribution of the latent codes of the training samples $q_\phi(\mathbf{z} | \mathbf{x})$ towards a unit Gaussian distribution $N(\mathbf{0}, \mathbf{I})$ and the distribution of the codes of the generated samples $q_\phi(\mathbf{z} | \hat{\mathbf{x}})$ away from $N(\mathbf{0}, \mathbf{I})$. The decoder tries to do the opposite to the generated samples. Furthermore, the encoder attempts to minimize reconstruction error $L_{\mathcal{X}}$ with L1 distance in sample space \mathcal{X} , and the decoder to minimize reconstruction error $L_{\mathcal{Z}}$ with cosine distance in latent code space \mathcal{Z} . Hence, as explained in detail

in [11], the full loss functions are as follows:

$$L_\phi = D_{\text{KL}}[q_\phi(\mathbf{z} | \mathbf{x}) \| N(\mathbf{0}, \mathbf{I})] - D_{\text{KL}}[q_\phi(\mathbf{z} | \hat{\mathbf{x}}) \| N(\mathbf{0}, \mathbf{I})] + \lambda_{\mathcal{X}} L_{\mathcal{X}}, \quad (1)$$

$$L_\theta = D_{\text{KL}}[q_\phi(\mathbf{z} | \hat{\mathbf{x}}) \| N(\mathbf{0}, \mathbf{I})] + \lambda_{\mathcal{Z}} L_{\mathcal{Z}}, \quad (2)$$

with D_{KL} denoting Kullback–Leibler divergence. The reconstruction loss terms are defined as:

$$L_{\mathcal{X}}(\theta, \phi) = \mathbb{E}_{\mathbf{x} \sim X} \|\mathbf{x} - \theta(\phi(\mathbf{x}))\|_1, \quad (3)$$

$$L_{\mathcal{Z}}(\theta, \phi) = \mathbb{E}_{\mathbf{z} \sim N(\mathbf{0}, \mathbf{I})} [1 - \mathbf{z}^T \phi(\theta(\mathbf{z}))]. \quad (4)$$

Vectors in \mathcal{Z} are always normalized to unity.

Contrasted to regular autoencoders, the second major aspect of PIONEER is the progressive growing of the network architecture during training, as follows. The encoder and decoder are divided into residual convolution/deconvolution building blocks that operate on separate resolutions (16×16 , 32×32 , ...). The training is divided into phases during which we only train the blocks that operate up to that resolution. Once that resolution is sufficiently learnt, we gradually fade in the block for the next level, and so on. (For more details, see [11, 17].)

When training on resolutions 128×128 or higher, we observe that around the time when the image generation results begin to get worse, the encoder tends to assign increasingly low KL divergence estimates for the training samples, and increasingly large ones for the generated samples. In other words, the encoder wins the game. We will keep this observation in mind, and now turn to the weight normalization schemes that underlie the training dynamics.

3.2. Simplification of the normalization scheme

In [11], three unrelated techniques are used to stabilize the training: (i) spectral normalization [29] in the encoder, and (ii) equalized learning rate [17] as well as (iii) pixel norm [17] in the decoder. However, there is no obvious reason why we could not replace (ii) and (iii) with (i). This makes the model more principled and, hypothetically, easier to train. In the spectral normalization approach, the spectral norm of each layer of the network is constrained directly during every computation pass, allowing the network to keep the Lipschitz constant under control. The operation does not regularize the network via learnable parameters, but re-scales network weights in a data-dependent manner.

However, if we only use spectral normalization, the learning may be stable on the low-resolution pre-training stages, but already at 64×64 resolution, we begin to see the effects of encoder overpowering the decoder. The training will become unstable shortly thereafter. We believe this is due to the increasingly large and noisy gradients that need to be regularized (Fig. 3).

3.3. Competing KL divergence terms

We now return to the KL terms. In general, the absolute values of the KL terms do not seem to always correlate with better generation results. Instead, the critical aspect seems to be the difference between them.

We thus set out to regularize this part of the training by adding a simple hinge loss to limit the gradient reward for the encoder. A major component of the gradient of the encoder comes from the gap between the KL terms. We wish to ensure that the encoder is not motivated to increase the gap too much, so we define a single margin term M_{gap} that defines the upper bound of the gap, and then modify Eq. (1) as follows into a hinge-loss form:

$$L_{\phi} = \max(-M_{\text{gap}}, D_{\text{KL}}[q_{\phi}(\mathbf{z} | \mathbf{x}) \| \mathcal{N}(\mathbf{0}, \mathbf{I})] - D_{\text{KL}}[q_{\phi}(\mathbf{z} | \hat{\mathbf{x}}) \| \mathcal{N}(\mathbf{0}, \mathbf{I})]) + \lambda_{\mathcal{X}} L_{\mathcal{X}} \quad (5)$$

Because the latter KL term is, in practice, almost always larger than the former, the gap is negative and needs to be bounded from below. Now, Eq. (5) alone would not care about the absolute values of the KL terms at all. However, since Eq. (2) remains unchanged, the decoder training provides the force that drives the $D_{\text{KL}}[q_{\phi}(\mathbf{z} | \hat{\mathbf{x}}) \| \mathcal{N}(\mathbf{0}, \mathbf{I})]$ lower. Combined with Eq. (5), the result is a force that pushes the other KL term lower, too (see Fig. 3 for an example of diverging KLs and the effect of bounding the gap).

After applying this change, the training becomes stable again, regardless of resolution, while using our simplified weight normalization scheme. There is no collapse of the training, and furthermore, we tend to see steady improvements well beyond the capacity of the original PIONEER.

With the approach in Eq. (5), instead of trying to reduce the learning rate to dampen the gradients, we can in fact *increase* it and train faster.

We note that the large gradients are not a problem in the early pre-training stages. On the contrary, applying a heavy-handed margin in the early stages will reduce the rate of learning too much. Hence, it is sufficient to only apply the margin after the pre-training. Alternatively, we could have defined the margin to be dependent on the progressive stage of the training, but more experiments should be done to confirm the generality of such margin choices.

3.4. Disentanglement of latent space

There are various definitions and ways to measure disentanglement of the latent space. One way of evaluating how the regions in the latent landscape correspond to the sample space is by focusing on finding directions in the latent space that correspond to specific factors of variation in the sample space, but in an unsupervised training setup, we might not have such factors known *a priori*. However, we can instead focus on identifying smooth transitions in the image sample space, quantitatively and visually.

Quantitatively, we can do this by measuring how smoothly the generated samples change while we move around in the latent space. This requires a good metric for measuring such changes between images, such as LPIPS [40]. Following the approach of [18], we can simply take samples of two random points in the latent space, look at a short vector segment that connects them, and generate images from both sides of the short segment. We can then proceed to measure the Perceptual Similarity between the points.

Visually, we can try to modify individual features of a new image, *e.g.* add a degree of smiling. To this end, we look for single-feature code vectors to add to the latent code of the image. Though the idea is now commonplace, there are variations for *e.g.* purely generative GANs or a supervised setup. Here, we take our existing model *trained without any class information*, a set A of images with the feature of interest, and a set B of images without it. *Requiring no additional training or optimization*, we take the difference between the mean latent code of each set and add the resulting 512-dimensional difference vector to the code of the real test image \mathbf{x}_{noF} , scaled to the desired intensity λ :

$$\mathbf{x}_F(A, B) = \theta(\phi(\mathbf{x}_{\text{noF}}) + \lambda \times [\mathbb{E}_{\mathbf{x} \sim A} \|\phi(\mathbf{x})\| - \mathbb{E}_{\mathbf{x} \sim B} \|\phi(\mathbf{x})\|]). \quad (6)$$

The modified latent code is decoded to an image with (or, with negative λ , without) the new feature (Fig. 6). (Contrast this procedure to GAN latent arithmetics, whereby *you can only transform random model-generated images*, unless you also set up an extra ad hoc network that learns to encode

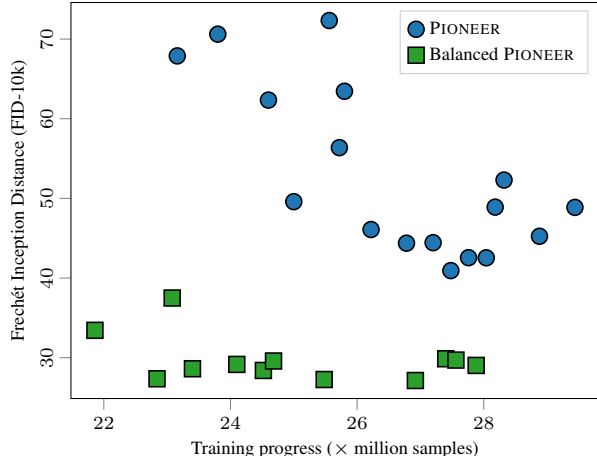


Figure 4. FID-10k values of CELEBA-HQ during training, with regular PIONEER and Balanced PIONEER. The FID measures the quality and diversity of generated images (smaller is better). The plot also shows the volatility in the regular PIONEER compared to the balanced.

your images into the GAN latent space, or run a separate optimization process for each input image.)

4. Experiments

Generative models can be used to create data samples, while encoder-decoder models can also modify them via latent space. These characteristics suggest that the natural ways of testing the model are by evaluating a batch of generated random samples, reconstructing new test samples, interpolating between two or more inputs in the latent space, or by analyzing the latent space directly.

The various ways of measuring generative models constitute an active field of research as such. To evaluate random samples, we are typically looking for both quality and diversity of the sampled distribution. The most often used methods are Fréchet inception distance (FID, [13]) and Inception Distance [32]. There are various shortcomings in these measures [2] but as long as we use identical sample size, FID appears to be a reasonably reliable tool for comparing different models. For easy comparison to the previous models, we measure against the training set (but see [23] for limitations).

To measure the conservation of features and identity in reconstructions, we use LPIPS [40] which correlates with human judgement more closely than, for example, the commonly used L2 distance or Structural Similarity measures [41]. Finally, to evaluate the quality of the latent space as such, we measure the Perceptual Path Length [18] and show interpolations between reconstructions of input images as well as feature modifications. The latter operations cannot result in high-quality samples unless the latent space is well-structured.

Table 1. Comparison of Fréchet Inception Distance (FID) and perceptual path length (PPL) of 256×256 images on CELEBA-HQ and LSUN dataset between Balanced PIONEER, regular PIONEER, PGGAN, IntroVAE and GLOW. Balanced PIONEER has the best PPL result, PGGAN has the best FID results. Improvement of the Balanced PIONEER over the regular PIONEER is clear on CELEBA-HQ. [14] provides the 256×256 FID of IntroVAE for LSUN Bedrooms but not for CELEBA-HQ (they provide it for 1024×1024 as 5.19, but with a more favorable train/test split). For other figures, the best-run results are shown. The GLOW model has not been shown to work with 256×256 figures on LSUN (the authors show qualitative result only at 128×128). FID is based on 50,000 batch of generated samples compared to training samples. Perceptual Path Length (PPL) was calculated with 100k samples, cropped to 128×128 ($\epsilon = 10^{-4}$). Pre-trained models for PGGAN and GLOW ($T = 0.9$ resulted in best FID) were used with default settings provided by the authors. For all numbers, **smaller is better**.

	FID (CELEBA-HQ)	FID (LSUN)	PPL (CELEBA-HQ)
PGGAN	8.03	8.34	229.2
IntroVAE	—	8.84	—
GLOW	68.93	—	219.6
PIONEER	39.17	18.39	155.2
Balanced PIONEER (ours)	25.25	17.89	146.2

Since PIONEER networks are most useful in the domain of high-resolution images ($128 \times 128 +$), we consider the CELEBA-HQ [17] and LSUN Bedrooms [38] datasets with images up to 1024×1024 and 256×256 resolution, respectively. CELEBA-HQ contains 30,000 images (where we use 27,000 / 3,000 split for training and testing images) while LSUN has its designated separate testing images.

We train the model progressively as in [11], allowing the last two pre-training phases (64×64 and 128×128) last 0.5–2 times longer than the earlier phases. The final phase is trained until convergence of the FID metric.

We train both the CELEBA-HQ model and the LSUN Bedrooms model for 8 days on two Nvidia V100 GPUs, up to 25.5M samples (epoch count is not useful here, since resolutions vary between epochs). As in [11] and [17], we reduce the batch size as we move to higher resolutions of the training, to fit within GPU memory limits. After the pre-training stages up to 64×64 , we switch on the margin ($m = 0.6$ for LSUN, $m = 0.2$ for CELEBA-HQ), and from 256×256 onwards, we fix the margin in both cases to $m = 0.4$ and also increase the learning rate (from 0.001 to 0.0015 for LSUN and 0.002 for CELEBA-HQ). The overall scale of m can be determined empirically from the behavior of KL divergence values. The fine-tuning is not necessary, but slightly improves the FID values. We optimize with ADAM [21] ($\beta_1 = 0$, $\beta_2 = 0.99$, and $\epsilon = 10^{-8}$). With any other inherent hyper-parameters and all architectural choices, we exactly follow [11] unless stated otherwise.



Figure 5. Generated random samples from CELEBA-HQ and LSUN Bedrooms. IntroVAE from [14] (CELEBA-HQ downsampled), the others uncurated.

4.1. LSUN Bedrooms

For LSUN Bedrooms, we show randomly generated samples in Fig. 5(b) at 256×256 resolution. In terms of visual comparison to, for example, [14], [17], or [10], it is hard to discern the differences between the models (see Fig. 5). However, visually comparing to [22] or [11], we can observe some mode collapse happening already at 128×128 in their results, and the authors do not provide 256×256 samples at all. We found that even the baseline PIONEER can indeed generate high-quality samples of LSUN Bedrooms at 256×256 ¹. The balanced PIONEER reaches slightly better FID figures with 30% less training steps in the final stage than PIONEER baseline (Fig. 4). In terms of FID scores, our Balanced PIONEER does not quite reach the state-of-the-art of [17] and [14]. However, the better performance of purely generative models such as [17] for random sampling is not directly comparable to that of encoder-based models.

4.2. CelebA-HQ

In [11], PIONEER was shown to generate relatively high-quality random samples in 256×256 resolution in CELEBA-HQ, but reconstructions only up to 128×128 (on regular CELEBA). With both the baseline and our Balanced PIONEER,

¹This may be due to fixing the PyTorch bug 12671[35] which prevented the spectral normalization from working on multi-GPU setup.

we show reconstructions at 256×256 . Balanced PIONEER is superior in both reconstructions (Fig. 2) and random sampling quality (Fig. 5(a) and Table 1).

While reconstruction of input images is not interesting as such, it serves as a proxy guarantee that the model at least handles the point in the latent space that represents the input image. We demonstrate sharp CELEBA-HQ reconstructions in Fig. 2. LPIPS score for 10k CELEBA-HQ samples (cropped at face area to 128×128 for more precise measurement) improved from 0.223 of the PIONEER baseline to 0.172 of our improved model (22.9% reduction).

4.3. Disentanglement measures

Finally, we evaluate whether the individual factors of variation in the training data are represented as directions in the latent space. We demonstrate this by examining interpolations between the reconstructions of input images (Fig. 1 and the Supplement) and feature manipulation (Fig. 6) The latent space remains smooth even for the relatively sparse dataset of CELEBA-HQ (with only 30k samples, as opposed to the 202k samples of CELEBA), biased towards females and a narrow set of face features and ages.

We measure the degree of disentanglement of the latent space with Perceptual Path Length [18]. In Table 1, we compare the PIONEER, Balanced PIONEER, PGGAN and

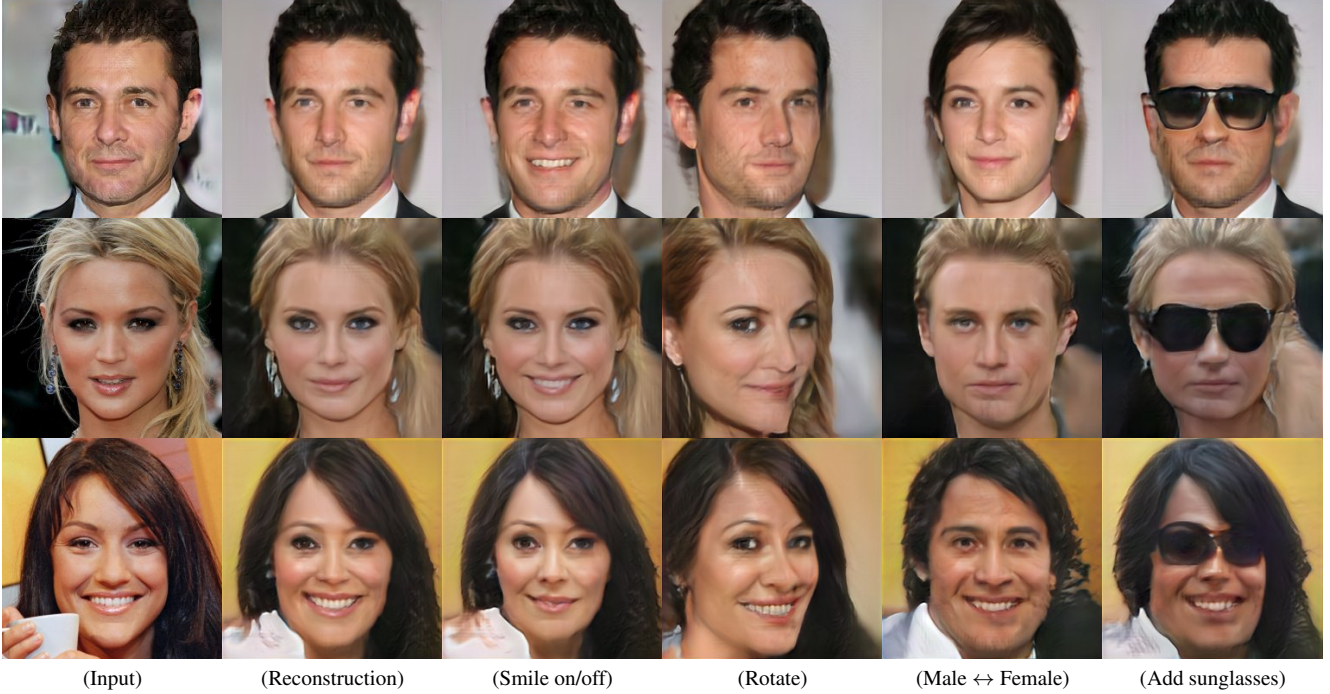


Figure 6. Examples of feature manipulation in 256×256 resolution CELEBA-HQ test set images that the model has not seen before, for attributes that the model did not know about during training. Column 1: the input; Column 2: the reconstruction; Columns 3–6: various added feature vectors. Each 512-dimensional feature vector was extracted after training as a simple arithmetical difference between the latent vector of 32 to 64 training set examples that contain and do not contain the feature. The difference vector was then added to the latent code of each new input image and decoded back into a result image. There is no *a priori* reason to assume that this would result in a valid image in the first place, nor that the feature would be transformed. Note that there is no class information in the training set, which means that during training, the model has to figure out the existence of these features from scratch. Only a well-structured latent space can explain the result. Here, the feature intensity scale λ varies between $[-2.0, 2.0]$. For smoothly increasing the intensity, please see the Supplement.

GLOW, using CELEBA-HQ image samples at 256×256 .

We sample 100,000 such pairs of points, decode them into images, and crop them around the center of the face, following [18]. The scaled expectation of the Perceptual Similarity value is, then, our ‘Perceptual Path Length’ (PPL) value. We find that the Balanced PIONEER outperforms the other models, which is not surprising, given its ability to interpolate well between most random input images.

5. Discussion and conclusions

In this paper, we have taken steps towards photographic image manipulation with PIONEER model, by substantially improving the model’s reconstructive capacity and latent space disentanglement, demonstrated in CELEBA-HQ, and, despite using a simpler model, slightly improved results with less training in LSUN Bedrooms. We proposed balancing of the model training in two respects; by bounding the difference between the competing KL divergence terms in the encoder, and by consistently using spectral normalization on both the encoder and the decoder. These steps made the model more principled, smoothed out strong oscillations in the encoder–decoder game, and prevented the encoder from

overpowering the decoder.

In resolutions not shown previously for this model family, the balanced training enabled us to show latent space interpolations (more examples in the Supplement) and extracted latent space features that visibly modify images in a realistic manner. In Table 1, we showed that the learned latent space structure is clearly better than the baselines, in terms of perceptual path length. FID scores are slightly worse than PGGAN and IntroVAE but better than the unbalanced PIONEER and GLOW.

The results suggest that AGE-based approaches are at least competitive with the ones based on GANs and VAEs. VAEs offer an explicit probability density function, and are less sensitive to the training minibatch size. However, they have been plagued by the problem of blurriness of generated images, and further research is needed to establish whether, for example, the approach in IntroVAE can solve this more generally. GLOW offers exact inference, but inferior FID. In future work, a training set more diverse than CELEBA-HQ, such as the FFHQ from [18], would also improve generality.

The PyTorch source code will be made available at <https://aaltovision.github.io/balanced-pioneer>.

Acknowledgments

We thank Tero Karras and Samuli Laine for advice about the metrics and Manu Paloniemi for early tests on PIONEER facial feature manipulation. We acknowledge the computational resources provided by the Aalto Science-IT project and CSC. Authors acknowledge funding from the Academy of Finland (grant numbers 308640 and 277685) and GenMind Ltd.

References

- [1] M. Arjovsky, S. Chintala, and L. Bottou. Wasserstein generative adversarial networks. In *International Conference on Machine Learning (ICML)*, 2017.
- [2] M. Binkowski, D. J. Sutherland, M. Arbel, and A. Gretton. Demystifying MMD GANs. In *International Conference on Learning Representations (ICLR)*, 2018.
- [3] A. Brock, J. Donahue, and K. Simonyan. Large scale gan training for high fidelity natural image synthesis. *CoRR*, abs/1809.11096, 2018.
- [4] A. Brock, T. Lim, J. M. Ritchie, and N. Weston. Neural photo editing with introspective adversarial networks. In *Proceedings of the International Conference on Learning Representations (ICLR)*, 2017.
- [5] T. Q. Chen, X. Li, R. B. Grosse, and D. K. Duvenaud. Isolating sources of disentanglement in variational autoencoders. *CoRR*, abs/1802.04942, 2018.
- [6] Y. Choi, M. Choi, M. Kim, J.-W. Ha, S. Kim, and J. Choo. StarGAN: Unified generative adversarial networks for multi-domain image-to-image translation. *arXiv preprint arXiv:1711.09020*, 2017.
- [7] J. Donahue, P. Krähenbühl, and T. Darrell. Adversarial feature learning. In *Proceedings of the International Conference on Learning Representations (ICLR)*, 2017.
- [8] V. Dumoulin, I. Belghazi, B. Poole, O. Mastropietro, A. Lamb, M. Arjovsky, and A. Courville. Adversarially learned inference. In *Proceedings of the International Conference on Learning Representations (ICLR)*, 2017.
- [9] I. J. Goodfellow, J. Pouget-Abadie, M. Mirza, B. Xu, D. Warde-Farley, S. Ozair, A. Courville, and Y. Bengio. Generative adversarial networks. In *Advances in Neural Information Processing Systems (NIPS)*, pages 2672–2680, 2014.
- [10] I. Gulrajani, F. Ahmed, M. Arjovsky, V. Dumoulin, and A. C. Courville. Improved training of wasserstein GANs. In *Advances in Neural Information Processing Systems (NIPS)*, pages 5767–5777. 2017.
- [11] A. Heljakka, A. Solin, and J. Kannala. Pioneer networks: Progressively growing generative autoencoder. In *Asian Conference on Computer Vision (ACCV)*, 2018.
- [12] A. Heljakka, A. Solin, and J. Kannala. Recursive chaining of reversible image-to-image translators for face aging. In *Proceedings of Advanced Concepts for Intelligent Vision Systems*, 2018.
- [13] M. Heusel, H. Ramsauer, T. Unterthiner, B. Nessler, and S. Hochreiter. GANs trained by a two time-scale update rule converge to a local Nash equilibrium. In *Advances in Neural Information Processing Systems (NIPS)*, pages 6626–6637, 2017.
- [14] H. Huang, Z. Li, R. He, Z. Sun, and T. Tan. IntroVAE: Introspective variational autoencoders for photographic image synthesis. In *Neural Information Processing Systems (NeurIPS)*, 2018.
- [15] P. Isola, J.-Y. Zhu, T. Zhou, and A. A. Efros. Image-to-image translation with conditional adversarial networks. In *CVPR*, 2017.
- [16] D. Jimenez Rezende, S. Mohamed, and D. Wierstra. Stochastic backpropagation and approximate inference in deep generative models. In *International Conference on Machine Learning (ICML)*, 2014.
- [17] T. Karras, T. Aila, S. Laine, and J. Lehtinen. Progressive growing of GANs for improved quality, stability, and variation. In *Proceedings of the International Conference on Learning Representations (ICLR)*, 2018.
- [18] T. Karras, S. Laine, and T. Aila. A style-based generator architecture for generative adversarial networks. *arXiv preprint arXiv:1812.04948*, 2018.
- [19] T. Kim, M. Cha, H. Kim, J. K. Lee, and J. Kim. Learning to discover cross-domain relations with generative adversarial networks. In *ICML*, volume 70 of *PMLR*, pages 1857–1865, 2017.
- [20] D. Kingma and M. Welling. Auto-encoding variational Bayes. In *Proceedings of the International Conference on Learning Representations (ICLR)*, 2014.
- [21] D. P. Kingma and J. Ba. Adam: A method for stochastic optimization. In *Proceedings of the International Conference on Learning Representations (ICLR)*, 2015.
- [22] D. P. Kingma and P. Dhariwal. Glow: Generative flow with invertible 1x1 convolutions. In *Advances in Neural Information Processing Systems (NeurIPS)*, pages 10236–10245. 2018.
- [23] K. Kurach, M. Lucic, X. Zhai, M. Michalski, and S. Gelly. The GAN landscape: Losses, architectures, regularization, and normalization. In *Reproducibility in Machine Learning Workshop at ICML 2018*, 2018.
- [24] G. Lample, N. Zeghidour, N. Usunier, A. Bordes, L. Denoyer, and M. Ranzato. Fader networks: Manipulating images by sliding attributes. In *Advances in Neural Information Processing Systems (NIPS)*, 2017.

- [25] A. Larsen, S. Kaae Sønderby, H. Larochelle, and O. Winther. Autoencoding beyond pixels using a learned similarity metric. In *Proceedings of the 33rd International Conference on Machine Learning*, pages 1558–1566, 2016.
- [26] A. Makhzani, J. Shlens, N. Jaitly, and I. Goodfellow. Adversarial autoencoders. In *Proceedings of the International Conference on Learning Representations (ICLR)*, 2016.
- [27] L. Mescheder, S. Nowozin, and A. Geiger. Adversarial variational Bayes: Unifying variational autoencoders and generative adversarial networks. In *Proceedings of the 34th International Conference on Machine Learning*, pages 2391–2400, 2017.
- [28] L. M. Mescheder. On the convergence properties of gan training. *CoRR*, abs/1801.04406, 2018.
- [29] T. Miyato, T. Kataoka, M. Koyama, and Y. Yoshida. Spectral normalization for generative adversarial networks. In *Proceedings of the International Conference on Learning Representations (ICLR)*, 2018.
- [30] M. Rosca, B. Lakshminarayanan, D. Warde-Farley, and S. Mohamed. Variational approaches for auto-encoding generative adversarial networks. *arXiv preprint arXiv:1706.04987*, 2017.
- [31] K. Roth, A. Lucchi, S. Nowozin, and T. Hofmann. Stabilizing training of generative adversarial networks through regularization. In *Advances in Neural Information Processing Systems*, pages 2018–2028, 2017.
- [32] T. Salimans, I. Goodfellow, W. Zaremba, V. Cheung, A. Radford, and X. Chen. Improved techniques for training GANs. In *Advances in Neural Information Processing Systems (NIPS)*, pages 2234–2242, 2016.
- [33] J. Tabor, S. Knop, P. Spurek, I. Podolak, M. Mazur, and S. Jastrzębski. Cramer–Wold AutoEncoder. *arXiv preprint arXiv:1805.09235*, 2018.
- [34] I. Tolstikhin, O. Bousquet, S. Gelly, and B. Schoelkopf. Wasserstein auto-encoders. *CoRR*, abs/1711.01558, 2018.
- [35] Tongzhou Wang. Fix SpectralNorm with DataParallel 12671. <https://github.com/pytorch/pytorch/pull/12671>. GitHub repository.
- [36] D. Ulyanov, A. Vedaldi, and V. Lempitsky. It takes (only) two: Adversarial generator-encoder networks. In *Proceedings of the Thirty-Second AAAI Conference on Artificial Intelligence (AAAI-18)*, pages 1250–1257, 2018.
- [37] Z. Yi, H. Zhang, P. Tan, and M. Gong. DualGAN: Unsupervised dual learning for image-to-image translation. In *ICCV*, 2017.
- [38] F. Yu, A. Seff, Y. Zhang, S. Song, T. Funkhouser, and J. Xiao. LSUN: Construction of a large-scale image dataset using deep learning with humans in the loop. *arXiv preprint arXiv:1506.03365*, 2015.
- [39] H. Zhang, T. Xu, H. Li, S. Zhang, X. Wang, X. Huang, and D. Metaxas. StackGAN: Text to photo-realistic image synthesis with stacked generative adversarial networks. In *Proceedings of the International Conference on Computer Vision (ICCV)*, 2017.
- [40] R. Zhang, P. Isola, A. A. Efros, E. Shechtman, and O. Wang. The unreasonable effectiveness of deep features as a perceptual metric. *CoRR*, abs/1801.03924, 2018.
- [41] W. Zhou, A. C. Bovik, H. R. Sheikh, and E. P. Simoncelli. Image quality assessment: From error visibility to structural similarity. *IEEE Transactions on Image Processing*, 13(4):600–612, 2008.
- [42] J.-Y. Zhu, T. Park, P. Isola, and A. A. Efros. Unpaired image-to-image translation using cycle-consistent adversarial networks. In *ICCV*, 2017.

Supplementary material for Towards Photographic Image Manipulation with Balanced Growing of Generative Autoencoders

A. Training details

The architecture follows [11], so that the encoder and the decoder are symmetric, composed of residual blocks with two convolutional layer each, and 1×1 convolution for a skip connection. The final layer of the encoder contains a 4×4 filter that reduces the feature map into 512 channels on a 1×1 map that, flattened, represents the latent vector. Other filters are 3×3 . At each forward pass, the latent vector is normalized to unit length. Each block in the encoder halves the resolution of the input with stride equalling two, while each block of the decoder doubles it by upsampling and then running a convolution with stride equal to one.

The training proceeds via seven resolution phases, from 4×4 to 256×256 . During the first half of each phase, the skip connection of the most recently added residual block is gradually faded out. During the second half, the skip connection is off. During each phase up to 32×32 , the network sees a total of 2.4M image samples. The batch size generally halves for each consecutive phase to fit in GPU memory, with size 16 used for the final 256×256 stage. The pre-training phases 64×64 and 128×128 contained 3.5–6.2M samples so that the total sample count seen during pre-training for Balanced PIONEER (20.04M in CELEBA-HQ, 21.4M in LSUN) was below the total for baseline PIONEER.

Combinations of margin values in range $[0.2, 0.6]$ were tried for learning rates in range $[0.001, 0.002]$. For the balanced PIONEER, the results with the best FID reached for 256×256 resolution after seeing 27.3M training image samples were selected. This limit was chosen as it was the point around which the baseline PIONEER reached best FID (10k) values for LSUN Bedrooms, slightly earlier than its best value for CELEBA-HQ (at 27.5M). Applying lower margin values, or even a margin of 0.2 before 64×64 resolution stage, resulted in obvious training failure already by the end of the 64×64 stage. At the other extreme, applying very high margin values would nullify the effect of the margin.

Following [11, 17], we maintain a moving exponential running average for the weights of the generator, and use it as the de facto generator after the training. Any other hyper-parameters follow [11]. We optimize with ADAM [21] ($\beta_1 = 0$, $\beta_2 = 0.99$, and $\varepsilon = 10^{-8}$).

B. Feature manipulation

Following the method in Sec. 3.4, we take the same CELEBA-HQ model that was trained in a completely unsupervised manner, and apply the feature vectors from the latent space as in Fig. 6, but this time showing how each feature transforms the (reconstruction of the) input image gradually as a function of λ (Fig. 7). We also provide more examples of the features in Fig. 6 applied to other images, and other features computed with the same method, and their combinations (Fig. 8).

C. Latent space interpolations

We show 4-way interpolation examples for uncured CELEBA-HQ test set images, following the same method as used for Fig. 1, but with evenly spaced (spherical) interpolation between the reconstructions of each of the input images in the corners (Fig. 10–12). Fig. 11 represents a failure case.

D. Random samples

We show more random generated samples for CELEBA-HQ using Balanced PIONEER (ours) (Fig. 13), the baseline PIONEER (Fig. 14), GLOW (Fig. 15) and PGGAN (Fig. 16). Similarly, we show more random samples for LSUN using Balanced PIONEER (ours) (Fig. 17) and the baseline PIONEER (Fig. 18).

E. Reconstructions

We show more uncured examples of CELEBA-HQ reconstructions, comparing Balanced PIONEER (ours) against the baseline PIONEER (Fig. 19–20).

F. Feature transformation videos

The attached video (see <https://aaltovision.github.io/balanced-pioneer>) demonstrates various gradual feature transformations (as in Fig. 7). Each transformation shows cases λ varying on a subrange of $[-2.0, 2.0]$, applied on the original test set images shown in Fig. 21.

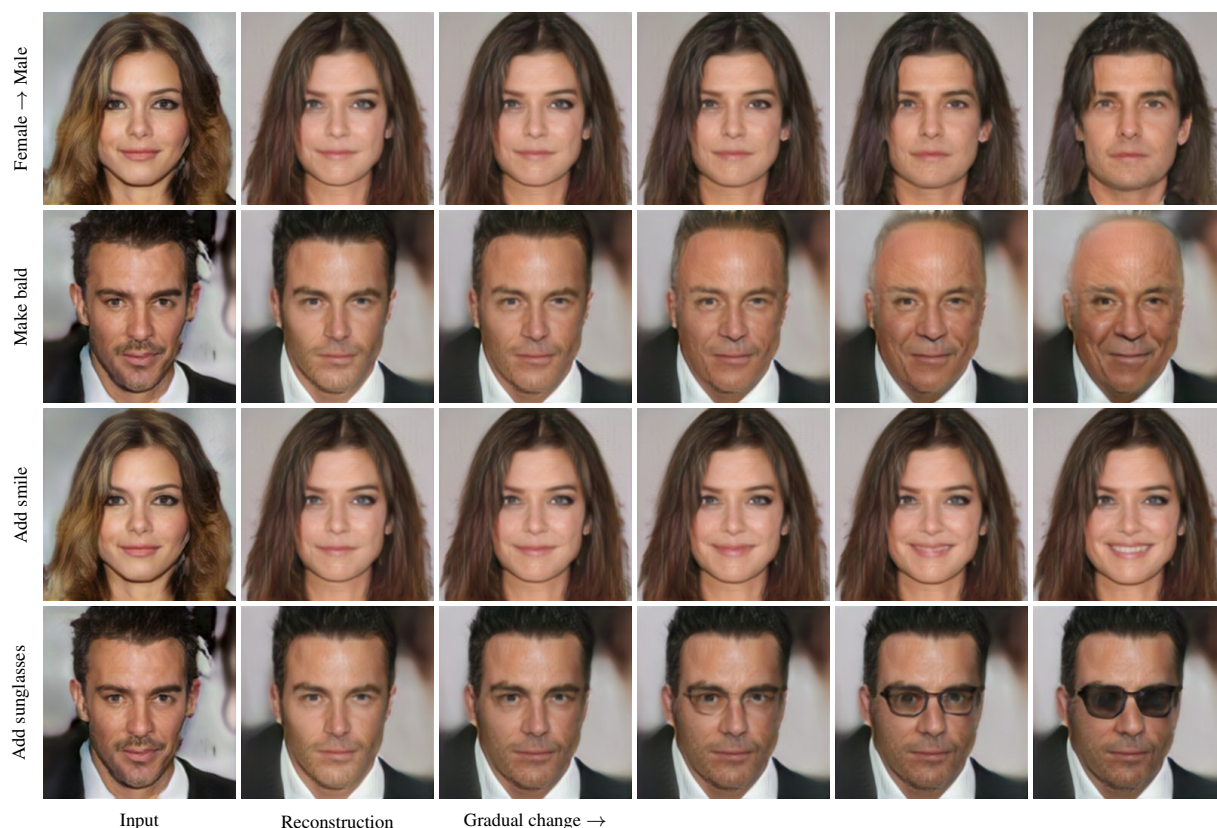


Figure 7. Balanced PIONEER gradual feature manipulation (CELEBA-HQ) at 256×256 resolution by increasing λ for a single feature. Column 1: Input; Column 2: Reconstruction ($\lambda = 0$); Columns 3–6: λ increasing. Row 1: Female \rightarrow Male; Row 2: Make bald; Row 3: Add smile; Row 4: Add sunglasses.

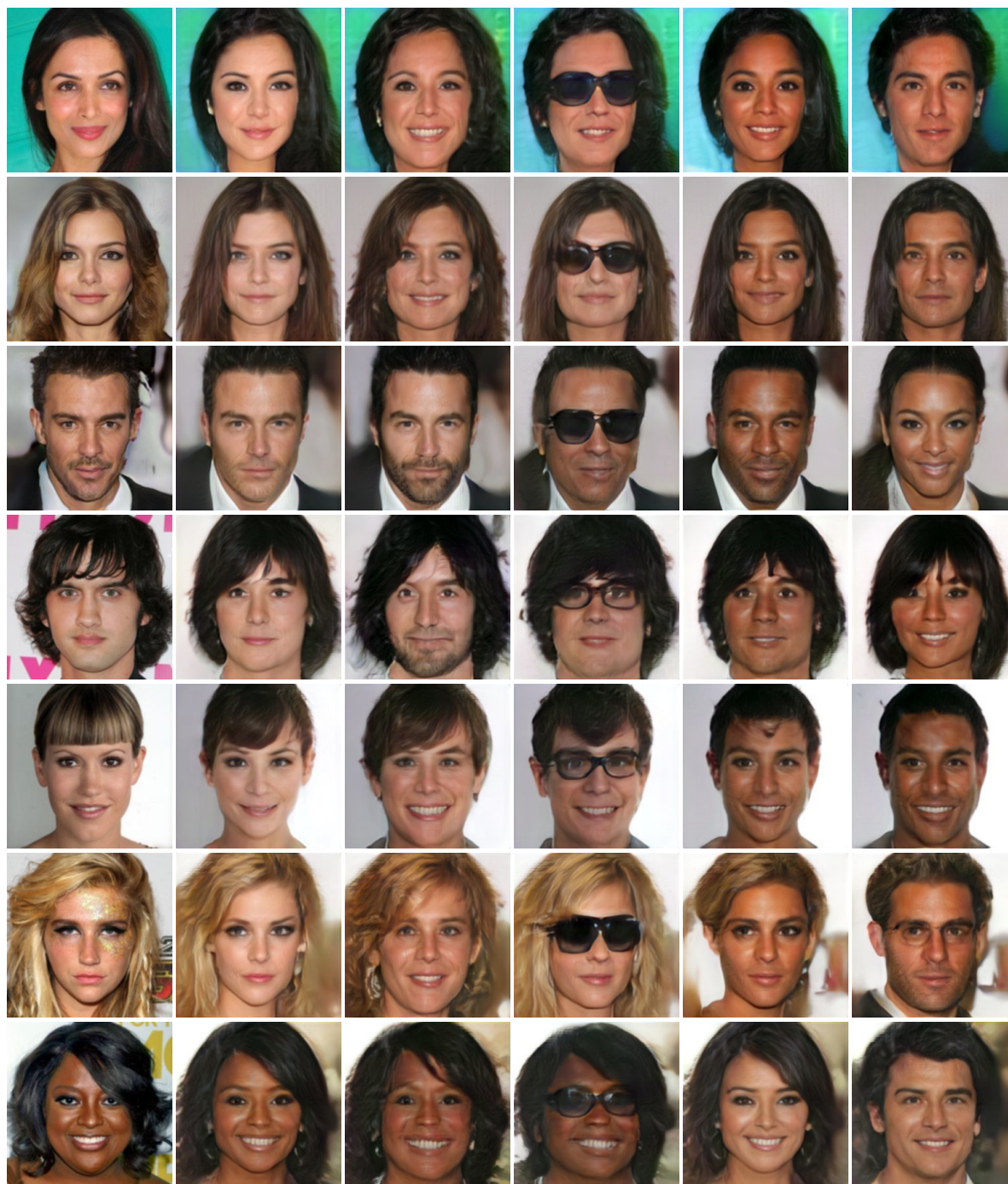


Figure 8. Balanced PIONEER discrete feature manipulation (CELEBA-HQ) at 256×256 resolution by adding various feature vectors. Column 1: Input; Column 2: Reconstruction ($\lambda = 0$); Column 3: Make older (females) or Add beard (males); Column 4: Make older + Add (sun)glasses; Column 5: Darken/whiten the skin; Column 6: Switch sex + Darken/whiten the skin.

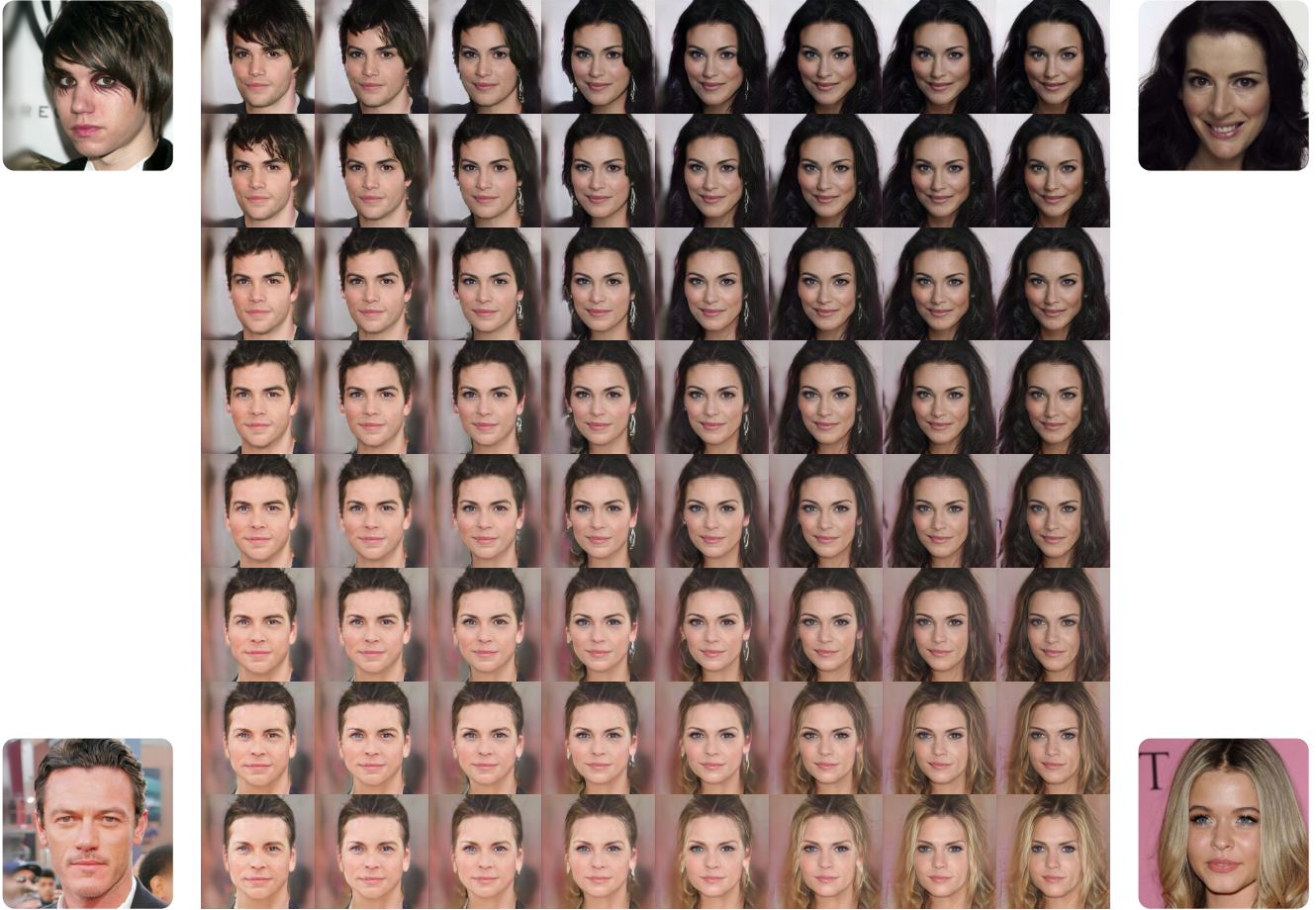


Figure 9. Interpolation between random uncensored test set CELEBA-HQ images in 256×256 . The model captures most of the salient features, although fails with some details such as the unusual make-up of the top-left person. Note that the moderate rotation angles of the faces are almost perfectly preserved, and the intermediate faces are rotated to the correct degree.

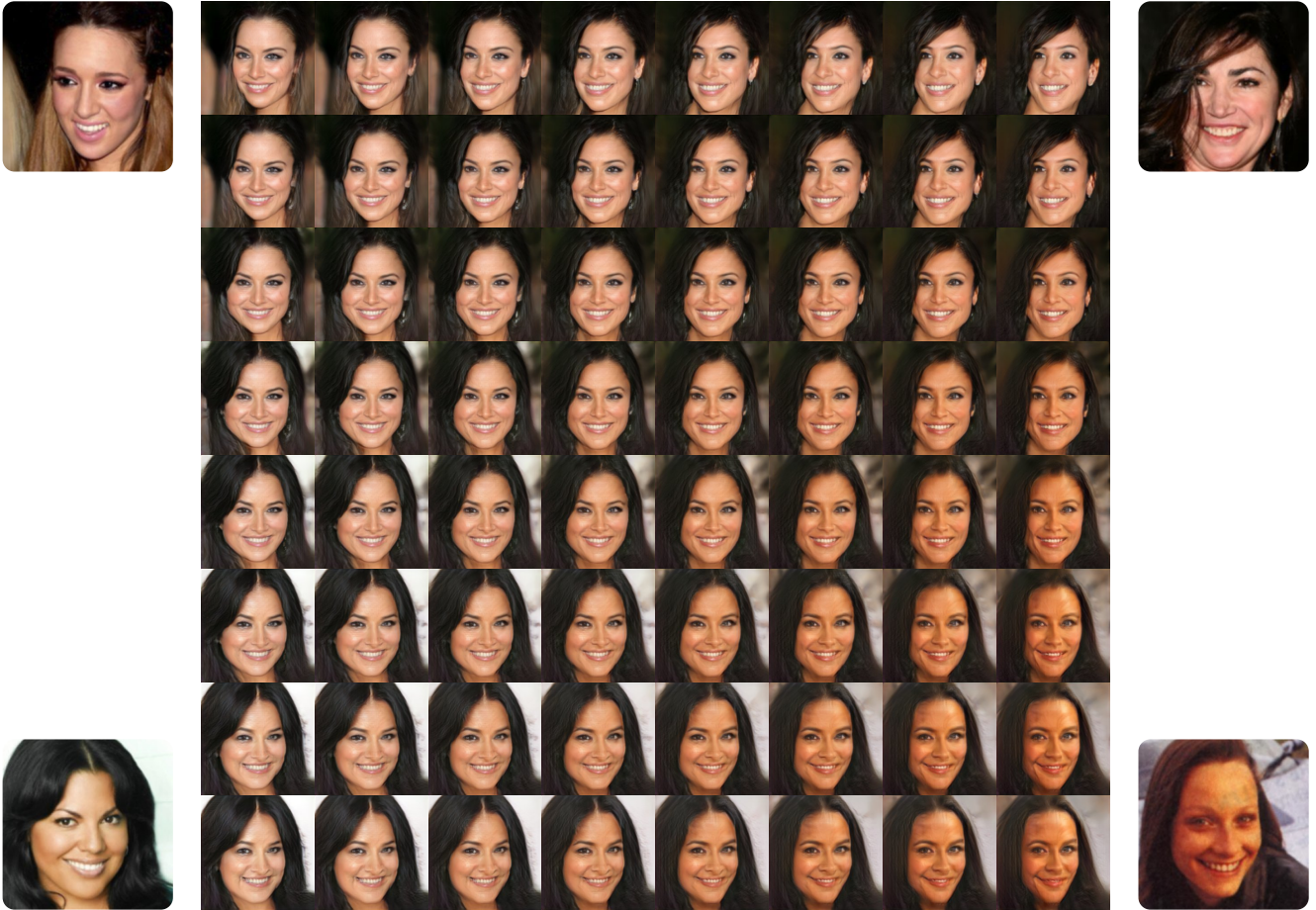


Figure 10. Interpolation between random uncured test set CELEBA-HQ images in 256×256 .



Figure 11. Interpolation between random uncured test set CELEBA-HQ images in 256×256 . Bottom-left image reconstruction is clearly inadequate.

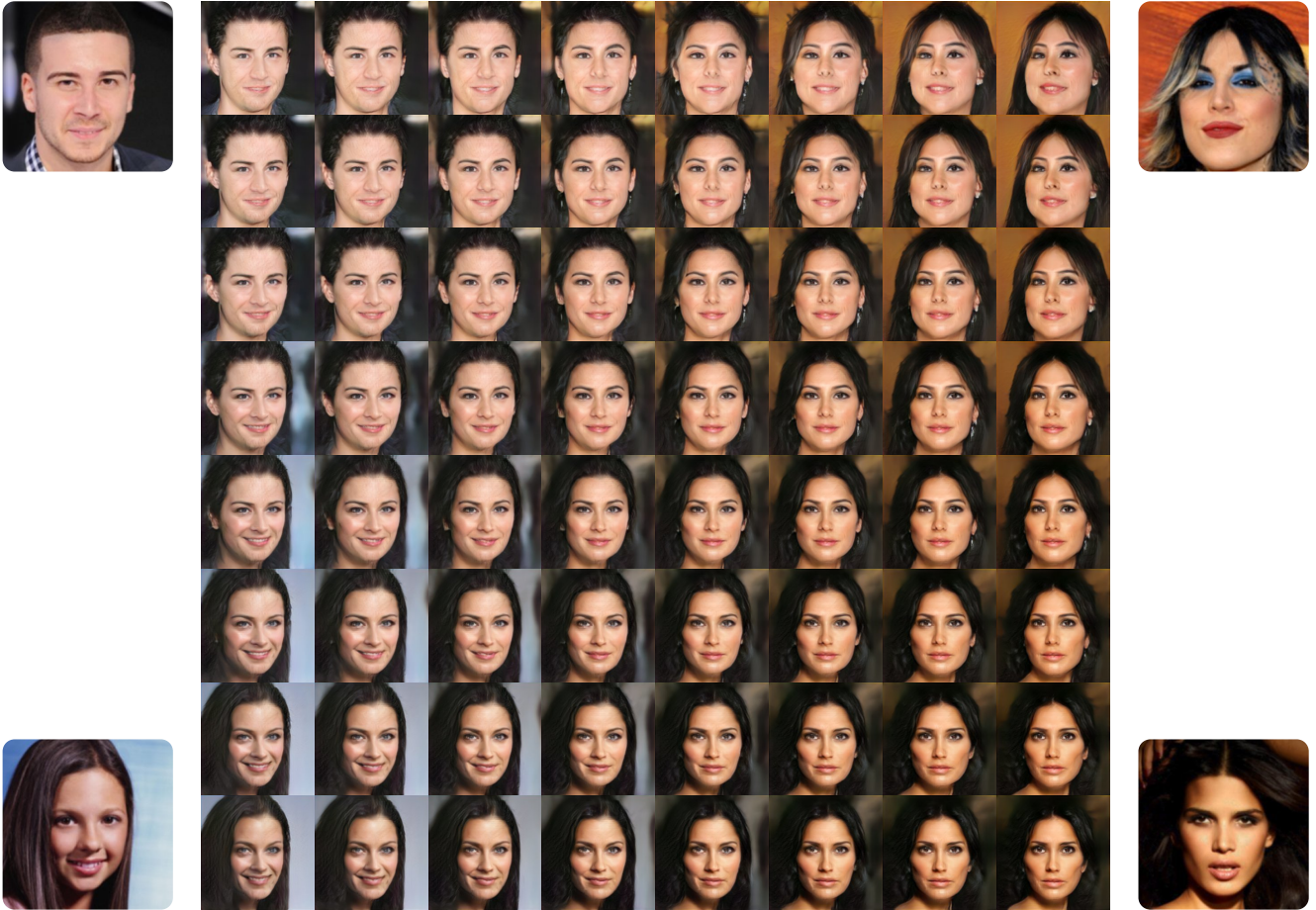


Figure 12. Interpolation between random uncured test set CELEBA-HQ images in 256×256 .



Figure 13. Balanced PIONEER (ours) random samples (CELEBA-HQ) at 256×256 resolution.



Figure 14. Baseline PIONEER random samples (CELEBA-HQ) at 256×256 resolution.



Figure 15. GLOW random samples (CELEBA-HQ) at 256×256 resolution, temperature $T = 0.7$.



Figure 16. Progressively Growing GAN (PGGAN) random samples (CELEBA-HQ) at 256×256 resolution.

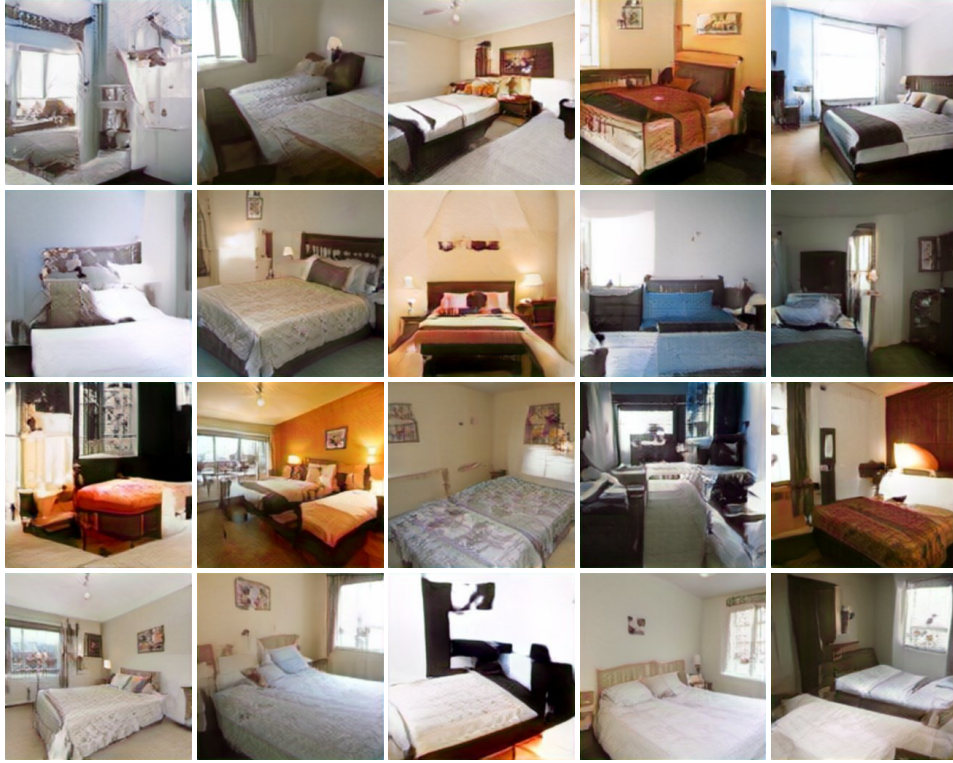


Figure 17. Balanced PIONEER (ours) random samples (LSUN Bedrooms) at 256×256 resolution.

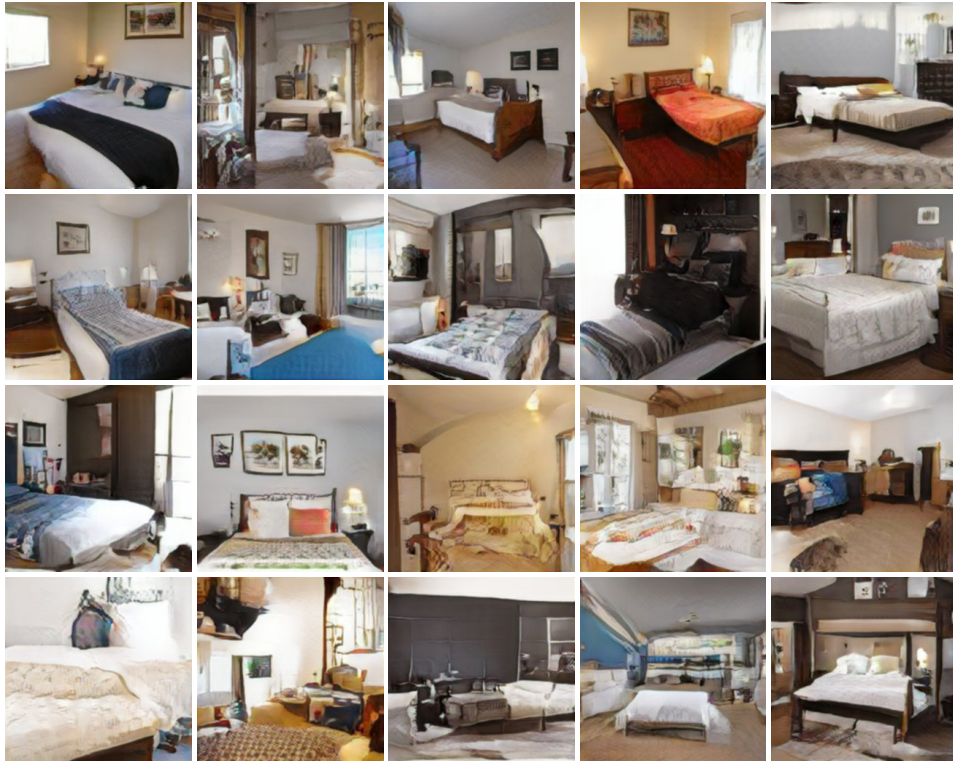


Figure 18. Baseline PIONEER random samples (LSUN Bedrooms) at 256×256 resolution.



Figure 19. More examples of reconstruction quality in 256×256 resolution with typical images from the CELEBA-HQ test set (top row), by our balanced PIONEER (middle) and baseline PIONEER (bottom). Here, the input images are encoded into 512-dimensional latent feature vector and decoded back to the original dimensionality (middle and bottom rows). The encoding-decoding of balanced PIONEER tends to preserve facial features, orientation, expressions, and hair style. Small mistakes can still be observed, especially in male subjects.

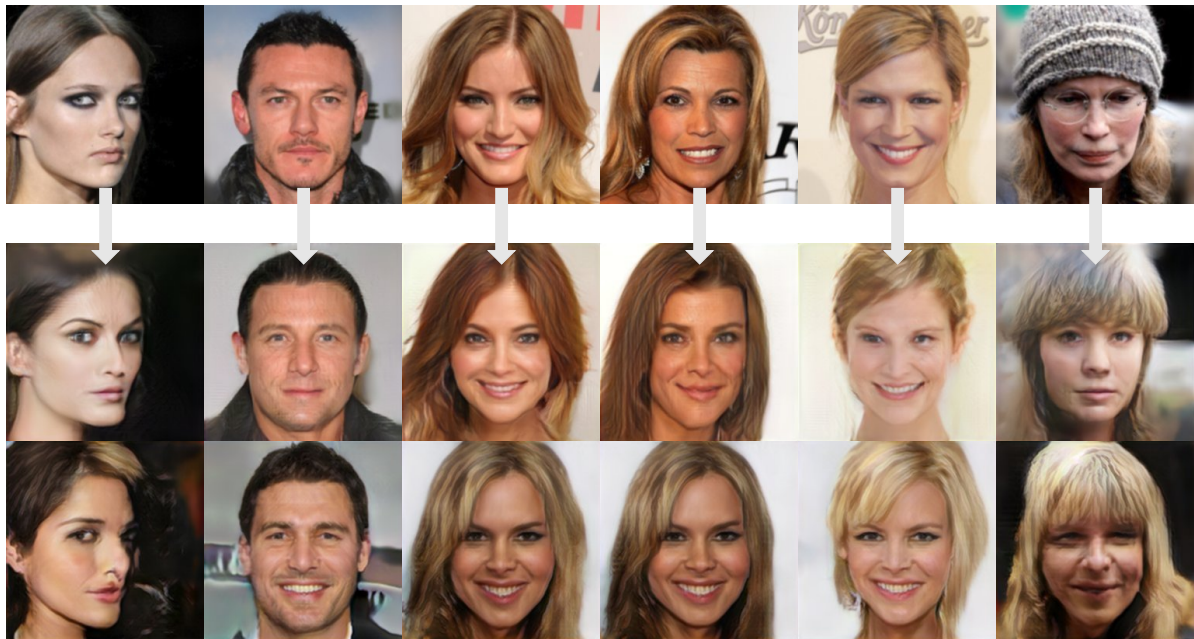


Figure 20. More examples of reconstruction quality in 256×256 resolution with typical images from the CELEBA-HQ test set (top row), by our balanced PIONEER (middle) and baseline PIONEER (bottom). Here, the input images are encoded into 512-dimensional latent feature vector and decoded back to the original dimensionality (middle and bottom rows). The encoding-decoding of balanced PIONEER tends to preserve facial features, orientation, expressions, and hair style. Small mistakes can still be observed, especially in male subjects.



Figure 21. CELEBA-HQ test set images used as input for the image transformation videos.